# The Growth and Elastoresistance Measurement of $FeTe_{1-x}Se_x$

Yue Shi

A thesis

submitted in partial fulfillment of the

requirements for the degree of

Master of Science

University of Washington

2018

Reading Committee:

Jiun-Haw Chu

Guozhong Cao

Program Authorized to Offer Degree:

Materials Science & Engineering

University of Washington

## Abstract

The Growth and Elastoresistance Measurement of $FeTe_{1-x}Se_x$

Yue Shi

Chair of the Supervisory Committee:

Assistant Professor Jiun-Haw Chu

Department of Physics

The iron-based superconductors (FeSCs) is one of the only two high temperature superconductors. Soon after its discovery, mounting experiments performed on several families of FeSCs demonstrate the existence of an electronic driven broken rotational symmetry phase, the nematic phase. As an integral part of the phase diagram, understanding the nature of the nematic phase is a key step to unveil the origin of high temperature superconductivity. The underlying charge or spin degree of freedom responsible for the nematic transition might be the same degree of freedom that gives rise the superconductivity and magnetic order. In this thesis, we use the elastoresistance technique to probe the nematic fluctuations in iron chalcogenide superconductors $FeTe_{1-x}Se_x$, which is one of the prototypes of FeSCs with the simplest crystal structure.

Specifically, two unique features of $FeTe_{1-x}Se_x$ distinguish it from the well-studied iron pnictides. First, the bicollinear antiferromagnetic order in FeTe is different from the collinear antiferromagnetic order in iron pnictides. Second, the nematic phase in FeSe forms without magnetic ordering, which is not the case in iron pnictides. Consequently, a systematic study of the $FeTe_{1-x}Se_x$ family will provide important insights into the universal role played by the nematic fluctuations.

In my thesis, I first describe the synthesis and annealing procedures of $FeTe_{1-x}Se_x$ crystals. Then I introduce the theoretical background and experimental techniques of elastoresistance measurement for $B_{2g}$ symmetry channel of Tetragonal symmetry point group. Finally, I describe the measurement of strong nematic fluctuation in $FeTe_{1-x}Se_x$. Our results show that the nematic fluctuations increase as the Se doping concentration increase for $FeTe_{1-x}Se_x$ (x = 0 - 0.5). The sign of elastoresistivity coefficient $2m_{66}$ flips between the $FeTe_{0.8}Se_{0.2}$ and $FeTe_{0.7}Se_{0.3}$ from negative to positive. The bare nematic critical temperature $T^*$ extracted from the Curie-Weiss fitting of $2m_{66}$ are negative for all components measured in our experiments. With the Se doping concentration increase, the bare nematic critical temperature $T^*$ approaches to zero, which implies the existence of nematic quantum criticality at the optimally doping.

# TABLE OF CONTENTS

# LIST OF FIGURES

# LIST OF TABLES

# ACKNOWLEDGEMENTS

I would first like to express my sincere gratitude to my advisor, Jiun-Haw Chu, for his continued encouragement and patient guidance. His passionate and respectful attitude towards research work is always an inspiration for my everyday work. Under his guidance, I learned how to process the experiment and become more enjoyable in pursuing a scientific question. I'm very lucky and honored to be a member of his group.

I would also like to acknowledge Prof. Guozhong Cao, as a committee member of my thesis as well as my co-advisor at the Materials Science & Engineering Department. I am gratefully indebted to him for his very valuable comments on this thesis.

The successful development of this thesis would not have been possible without the help of my group members. Qianni Jiang is the one who gave me an exhaustive lab tour at the first time I came to the lab and taught me everything from basics. We also completed this project together in the past a half year. I learned so much from her. I sincerely appreciate her help and company; Paul, Josh, and Shua are senior Ph.D. students. They know everything about the lab and always answer my questions patiently. Zhong and Zhaoyu are Post-doctors joining lab a few months ago. Even we just worked together one quarter, their professionalism and diligence of work impressed me a lot. They are great models for me in research work. Tiema, Llham, Anna, Teddy are undergraduates who are fun to work with. Thanks for their company which makes my research work and life more colorful.

Finally, I must express my very profound gratitude to my parents and to my boyfriend Yang for providing me with unfailing support and continued encouragement throughout my years of study and through the process of doing the research and writing this thesis. This accomplishment would not have been possible without them. Thank you.

# Chapter 1. INTRODUCTION

## 1.1 BACKGROUND

In 2008, the discovery of superconductivity in $LaO_{1-x}F_xFeAs$ at 26K by Hideo Hosono's group simulated the global research of high-temperature iron-based superconductors[1]. Soon after, a rapid increase of $T_c$ has been achieved by replacing La with other rare-earth elements in $LaO_{1-x}F_xFeAs$ crystals[2-6]. The highest critical temperature reaches 55K, which was reported in $SmO_{1-x}F_xFeAs$ by Ren et al.[5].

So far, four major classes of iron-based superconductors (FeSCs) have been identified according to the crystal structures of their stoichiometric parent compounds: 11-type Fe (Te, Se, S), 111-type AFeAs ($A$ = alkali metal), 122-type $AeFe_2As_2$ ($Ae$ = Ba, Sr, or Ca), 1111-type LnOFeAs ($Ln$ = rare earth). As Fig. 1.1 shown, crystal structures of four classes of parent compounds of FeSCs share a similar layered structure. The planar layers of iron atoms were joined by tetrahedrally coordinated pnictogen (As, P) or chalcogen (Se, S, Te) atoms, and the layers form a stacked structure. Between the stacked layers, alkali, alkaline-earth, rare-earth or oxygen/fluorine atoms donate electrons and serve as spacer layers. It is widely believed that the high temperature superconductivity originates within the common iron layers, like the copper-oxygen building block in the cuprate high-temperature superconductors.

The electronic structure of FeSCs has been studied intensively[7-9]. Most of the iron-based superconductors share a similar structure of the Fermi surfaces, except the heavily doped case of $K_xFe_{2-y}Se_2$ and related compounds, in which the hole pockets near the Brillouin zone center are absent[10, 11]. Fig. 1.2 shows the Fermi surfaces of FeSe as a representative of FeSCs. The Fermi surfaces are consisted of two electron cylinders centered at the Brillouin zone corner, compensated by three hole-like Fermi surfaces around the Brillouin zone center.

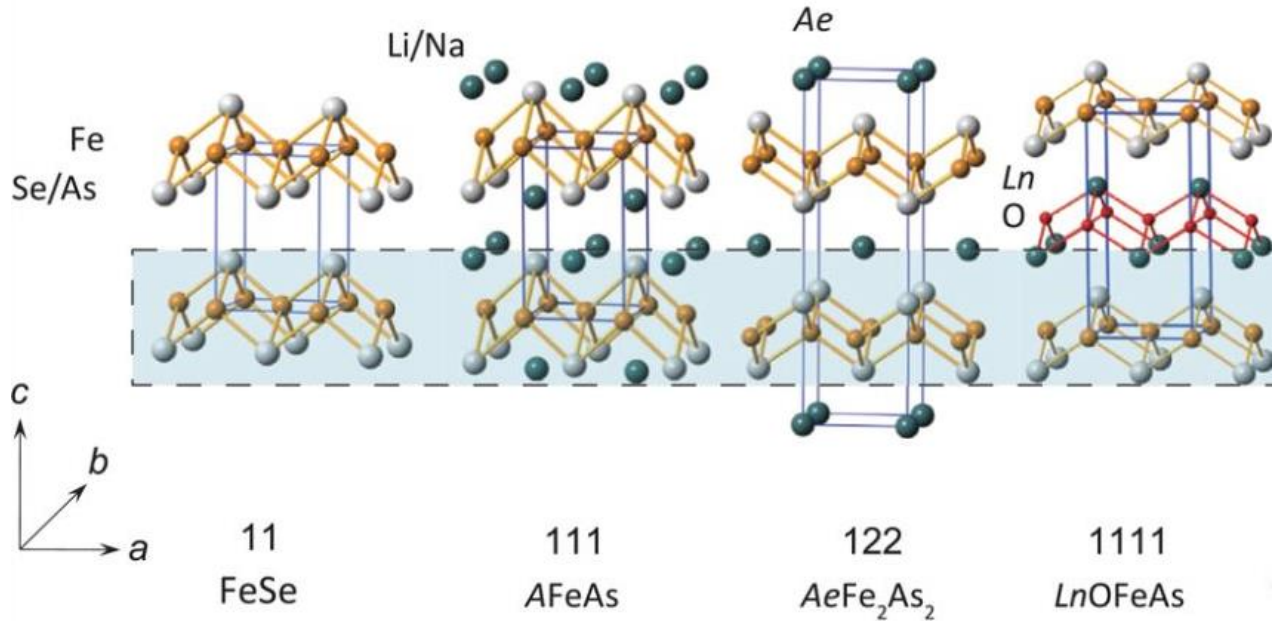


Figure 1.1. The schematic view of four classes crystal structures of FeSCs parent compounds: 11-type, 111-type, 122-type, 1111-type. A, Ae and Ln denote the alkali, alkali-earth, and lanthanide atoms. Iron tetragonal lattice coordinated with pnictide/chalcogenide atoms form the superconducting layers[12].

The phase diagrams of FeSCs are qualitatively similar to several other unconventional superconductors. In particular, the stoichiometric parent compounds of 1111 and 122 iron pnictides host broken symmetry phases. It is paramagnetic at room temperature, but when temperature decreases the paramagnetic state turns into the antiferromagnetic phase at Neel temperature $T_N$. Significantly, the antiferromagnetic transition is always accompanied with or preceded by a tetragonal-to-orthorhombic structural transition at $T_S$. The $T_N$, $T_S$ decrease and superconductivity appears by chemical doping[13, 14] or by applying pressure[15]. The highest superconducting temperature always appears around the suppression of antiferromagnetic phase.

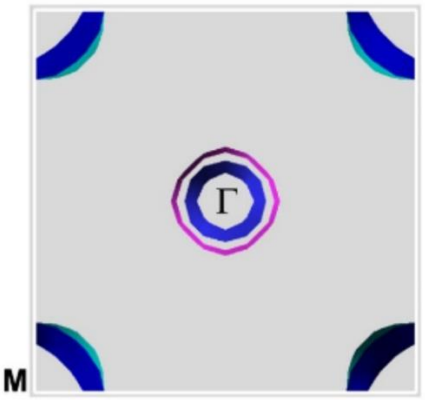


Figure 1.2. The Fermi surface structure of FeSe from the non-spin polarized calculation with the LDA[16]. The hole-like Fermi surface sheets are centered on the Γ point, the electron-like Fermi surface sheets are at the M point.

The structural transition, of pnictide superconductors breaks the point group rotational symmetry of crystal spontaneously without breaking translational or time-reversal symmetry. Because the order parameter of this transition is similar to the order parameter of the nematic phase of the liquid crystal[17], this transition is named as the 'electronic nematic phase'. Meanwhile, the theoretical work suggested that the tetragonal-to-orthorhombic transition may be derived by electronic rather than lattice degrees of freedom, which was confirmed by several experiments[18, 19]. One experimental evidence is that the anisotropy in electronic properties, such as resistivity is much larger than the anisotropy of the lattice parameters. If the nematic transition is of the electronic origin, it is likely emerging from the same quasiparticles that give rise to superconductivity and magnetic order[20]. So far, one open question is whether the nematic phase is derived from charge/orbital fluctuations[21, 22] or spin fluctuations[23-25]. The charge/orbital fluctuations also favors a sign-preserving s-wave superconducting pairing whereas spin fluctuation favors a sign-changing s-wave or d-wave state[20]. Previous inelastic neutron scattering

experiments suggested the spin fluctuations associated with suppressed antiferromagnetism play an important role in superconducting pairing[26, 27].

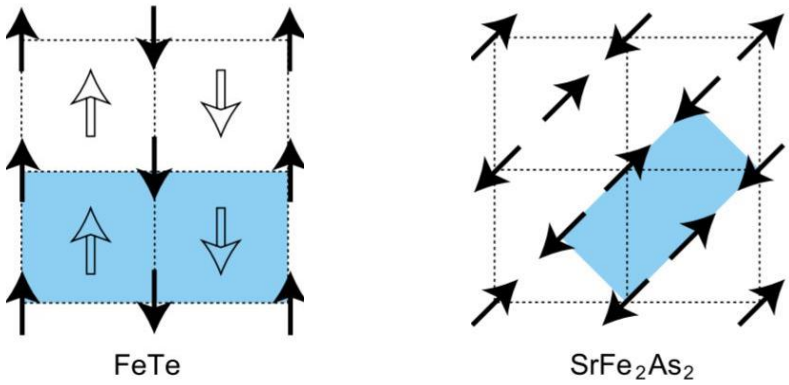


Figure 1.3. The schematic diagram illustrating the in-plane antiferromagnetic order of FeTe and $SrFe_2As_2$. The shaded area indicates the magnetic unit cell[28].

Here, we study nematic susceptibility of iron chalcogenide superconductors $FeTe_{1-x}Se_x$ by measuring its elastoresistance coefficient. The elastoresistance coefficient of the samples can be calculated from the resistivity anisotropy induced by in-plane anisotropic strain. The elastoresistance measurement method is also a powerful tool to probe the origin of various broken symmetry phases.

## 1.2 $FeTe_{1-x}Se_x$

In my thesis, I mainly focus on the chalcogenide superconductors $FeTe_{1-x}Se_x$ (x = 0, 0.1, 0.2, 0.3, 0.4, 0.5) to understand the underlying mechanism of electronic nematic phase. It is an ideal candidate with the simplest crystal structure among the FeSCs without the toxic Arsenic element.

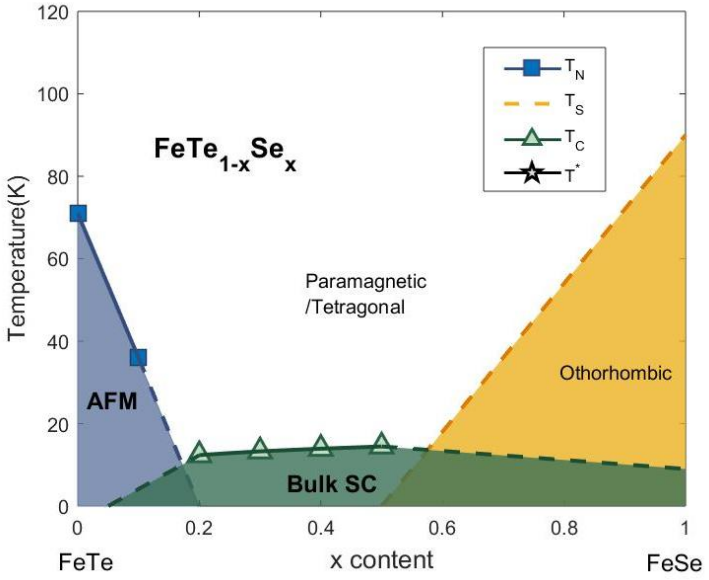


Figure 1.4. The phase diagram of $FeTe_{1-x}Se_x$. The dotted lines in the phase diagram are extracted from previous literature[29, 30], the markers and solid lines are extracted from resistivity measurements.

The parent compound FeTe at room temperature has a $Cu_2Sb$-type structure (space group of $P4/nmm$). As Fig. 1.4 shown, FeTe is not a superconductor and exhibits a spin-density wave (SDW) ground state at low temperature. As the temperature cools down, FeTe exhibits a tetragonal-to-monoclinic lattice distortion in the $[100]_T$ plane at around 70K, which is accompanied by a Neel paramagnetic-to-antiferromagnetic transition. With Se doping concentration increases, Se doping suppresses long-ranged antiferromagnetic order and induces superconductivity. The $T_c$ goes up to 14K at $x = 0.4$[31]. For $0 < x < 0.1$, there is no bulk superconductivity for $FeTe_{1-x}Se_x$ even though the structural and magnetic transition are simultaneously suppressed by Se doping. The bulk superconductivity appears started from $x = 0.4$ till pure FeSe below the critical temperature. Optimal doping occurs in the range of $0.4 < x < 0.5$[32, 33], where the structural and magnetic transition are fully suppressed. The phase diagram of $FeTe_{1-x}Se_x$ is similar with other FeSCs, however, the antiferromagnetic order of FeTe is

different from the collinear antiferromagnetic order of iron pnictide superconductors. The bicollinear AFM order in FeTe is characterized by a wave vector $Q_n = (\pi, 0)$, while the collinear AFM order in iron pnictides is characterized by an in-plane propagation wave vector $Q_n = (\pi, \pi)$. The Fig. 1.3 shows the schematic view of the in-plane antiferromagnetic order of FeTe and $SrFe_2As_2$.

In this thesis, I describe crystal synthesis procedures for the crystals I used in the project and present the methods we used to anneal the crystal samples in Chapter 2. In Chapter 3, I present the theoretical background and experiment techniques of elastoresistance measurement. Finally, I describe the experiments results. Through the elastoresistance measurement of $FeTe_{1-x}Se_x$ (x = 0, 0.1, 0.2, 0.3, 0.4, 0.5), we measured the elastoresistivity coefficient $2m_{66}$ for all components. The elastoresistivity coefficient $2m_{66}$, which is proportional to the strength of nematic fluctuations, increases as the Selenium doping concentration increases and reaches a maximum for $FeTe_{0.5}Se_{0.5}$. The sign of $2m_{66}$ flips between $FeTe_{0.8}Se_{0.2}$ and $FeTe_{0.7}Se_{0.3}$ from negative to positive. The bare nematic critical temperatures $T^*$ are negative for all components and approach zero with the Se doping increase, which implies the nematic quantum criticality at optimally doping, which is likely related to the nematic transition in FeSe.

# Chapter 2. MATERIAL SYNTHESIS

In this chapter, I first present the procedures for synthesizing single crystals of iron chalcogenide superconductors-$FeTe_{1-x}Se_x$ (x = 0, 0.1, 0.2, 0.3, 0.4, 0.5). Then I present the procedures and results of Se annealing that removes the interlayer excess iron atoms of $FeTe_{1-x}Se_x$ crystals.

## 2.1 GROWTH METHODS

Single crystals of $FeTe_{1-x}Se_x$ (x = 0, 0.1, 0.2, 0.3, 0.4, 0.5) were grown by the modified Bridgman method. The elements, Iron Powder (99.999%, Aldrich), Selenium Shot (99.999%, 2-5mm, Alfa Aesar), Tellurium Shot (99.999%, 2-5mm, Alfa Aesar) were stoichiometrically loaded into the evacuated quartz ampoules. We obtained high quality single crystals from two slightly different growth methods. In the first method the crystals were grown in vertically placed sealed quartz ampoules in the box furnace (MTI, KSL-1200X-J-UL). The temperature was ramped from room temperature to 680℃ for 6 hours, then increased up to 920℃ in 12 hours. After melting, the temperature was held for 3 hours and cooled down to 400℃ with a rate of 2 ℃/h. At last, the samples cool down to room temperature quickly. In the second method, the crystals were grown in a one zone tube furnace (Thermo Scientific, TF55030A). The sealed quartz ampules horizontally lie in the tube furnace. One side was placed in the center of the furnace near the thermometer while the other side is far away off the center. This temperature gradient along the ampule is beneficial for the formation of large crystalline grains. The outgrowth crystal can be large as $1\text{cm} \times 1\text{cm}$. The total weight of elements in one ampule is less than 2 grams, in order to reduce the risk of Se vapor rupturing the quartz ampule.

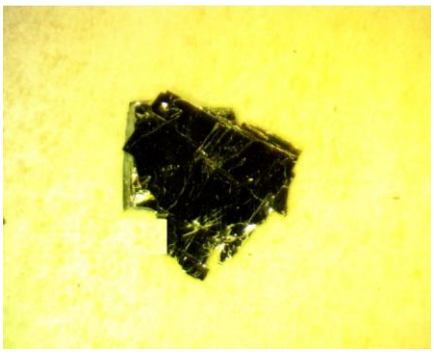

Figure 2.1. The $FeTe_{0.7}Se_{0.3}$ bulk crystal grown by the modified Bridgman method. The crystal has a plate-like morphology with a cleavage plane along $[100]_T$. The as-grown crystal can be as large as 1cm×1cm.

The obtained crystals have a plate-like morphology with a cleavage plane perpendicular to $[001]_T$. As Fig. 2.1 shown, the $FeTe_{0.7}Se_{0.3}$ (nominal Se content) crystal grown from the modified Bridgman method with the plate perpendicular to $[001]_T$ is shiny as reflected.

There is a width of formation of FeTe in the Fe-Te binary phase diagram. As grown crystals normally came out with excess iron atoms positioned in interstitial layers, especially in underdoped compositions. Excess iron concentration can be as high as 7-25% depending on growth conditions[34]. Excess iron positioned in the interstitial layer contributes excess electrons to the in-plane Fe which enhances the tendency towards the double-stripe antiferromagnetic state, therefore suppresses the superconducting temperature of samples. Furthermore, they form magnetic ions that are strongly coupled to the in-plane Fe, which further suppresses other magnetic instabilities[35]. Fig. 2.2 show the temperature-dependence of resistance for $FeTe_{0.7}Se_{0.3}$. Because of the excess iron, there is an upturn of resistance above the superconducting critical temperature $T_c$ and the superconducting transition is broad. It's necessary to find an effective way to reduce the excess iron concentration in order to study its intrinsic properties.

## 2.2 ANNEAL METHODS

Here we used several ways to anneal $FeTe_{1-x}Se_x$ crystals. First, we tried the vacuum anneal method. Crystal was cut into shiny thin chips along cleavage plate with less than $1mm$ thickness in order to get sufficient reaction. Then chips were sealed in quartz ampule under vacuum and put in the furnace under 400℃ for 10 days. We also annealed crystal chips under Se atmosphere. Thin crystal chips were sealed with Se powder together under vacuum in the crucible double-packed in the evacuated quartz ampule. As Fig. 2.2 shown, the Se powder was loaded in the bottom crucible, the crystal chips were placed in the middle crucible. When the temperature goes up to 400 ℃, the crystal chips were annealed under Se atmosphere for 48 hours for sufficient reaction. The annealing process would dramatically damage the crystal surface. Heavy cleaving and cutting afterwards were needed in order to obtain nice single crystals with shiny surfaces for transport measurements.

Fig. 2.3 shows the temperature-dependence of resistance for the as-grown and post-anneal crystal of $FeTe_{0.6}Se_{0.4}$. After annealing in Se vapor, the resistance upturn above the critical temperature disappeared and the superconducting transition becomes sharper. The critical temperature of the annealed sample is about 1K higher than that of the as-grown sample.

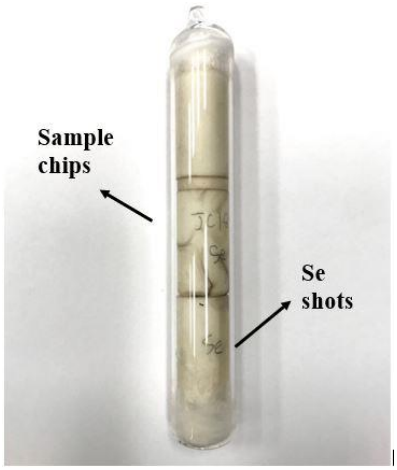


Figure 2.2. The picture of evacuated quartz ampule used in Se annealing method. The Se powder is loaded in the bottom crucible and the crystal chips are placed in the middle crucible. After the temperature reached 400℃, Se vapor becomes saturated in the quartz ampule, and the crystal chips were sufficiently annealed under Se atmosphere.

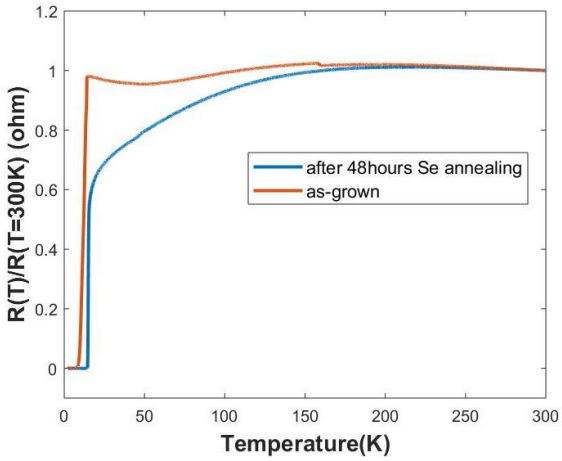


Figure 2.3. The temperature-dependent normalized resistance (R(T)/R(T = 300K)) of as grown and annealed $FeTe_{0.6}Se_{0.4}$. For the as-grown sample, there is an upturn in resistance just above the superconducting critical temperature, which comes from the effect of disorder due to interstitial excess iron. The resistance upturn disappeared after annealing the sample 48hrs under Se atmosphere.

# Chapter 3. ELASTORESISTANCE MEASUREMENT

## 3.1 THEORETICAL BACKGROUND

In this chapter, I present the definition of the elastoresistivity tensor and the relationship between the elastoresistivity coefficient $2m_{66}$ and the $B_{2g}$ nematic susceptibility. I also introduce the modified Montgomery method for elastoresistance measurement and the Curie-Weiss fitting for data analysis.

### 3.1.1 *Elastoresistivity Tensor*

The elastoresistance measurement refers to the measurement of relative change of resistivity of a crystal induced by strain. Here, the resistivity change can be defined as the strained-induced resistivity subtracted by the zero-strain resistivity [36]:

$$\Delta\rho_{\alpha\beta} = \rho_{\alpha\beta}(\epsilon) - \rho_{\alpha\beta}(\epsilon = 0) \tag{3-1}$$

Then the normalized resistivity can be expressed as:

$$(\Delta\rho/\rho)_{\alpha\beta} = \Delta\rho_{\alpha\beta}/\sqrt{\rho_{\alpha\alpha}\cdot\rho_{\beta\beta}} \tag{3-2}$$

Without magnetic fields in this measurement, the Onsager reciprocal relation holds for the electric conductivity. The resistivity and strain become symmetric tensors can be reduced to 6 independent components[36, 37]:

$$\begin{aligned}&(\Delta\rho/\rho)_{\alpha\beta}\\ &= \left((\Delta\rho/\rho)_{xx}, (\Delta\rho/\rho)_{yy}, (\Delta\rho/\rho)_{zz}, (\Delta\rho/\rho)_{yz}, (\Delta\rho/\rho)_{zx}, (\Delta\rho/\rho)_{xy}\right)\end{aligned} \tag{3-3}$$

$$\epsilon_{\gamma\delta} = \left(\epsilon_{xx}, \epsilon_{yy}, \epsilon_{zz}, \epsilon_{yz}, \epsilon_{zx}, \epsilon_{xy}\right) \tag{3-4}$$

The elastoresistance tensor $m_{\alpha\beta,\gamma\delta}$ relates two second rank tensors, the strain $\epsilon_{\gamma\delta}$ and the strain induced resistivity change $(\Delta\rho/\rho)_{\alpha\beta}$. Therefore it is a forth rank tensor[36]:

$$m_{\alpha\beta,\gamma\delta}(H) = \left.\frac{\partial(\Delta\rho/\rho)_{\alpha\beta}}{\partial\epsilon_{\gamma\delta}}\right|_{\epsilon=0} \quad 3\text{-}5$$

Using the Voigt notation, the elastoresistivity can be expressed as a pseudo-second rank tensor:

$$m_{ik} = \begin{pmatrix} m_{11} & m_{12} & m_{13} & m_{14} & m_{15} & m_{16} \\ m_{21} & m_{22} & m_{23} & m_{24} & m_{25} & m_{26} \\ m_{31} & m_{32} & m_{33} & m_{34} & m_{35} & m_{36} \\ m_{41} & m_{42} & m_{43} & m_{44} & m_{45} & m_{46} \\ m_{51} & m_{52} & m_{53} & m_{54} & m_{55} & m_{56} \\ m_{61} & m_{62} & m_{63} & m_{64} & m_{65} & m_{66} \end{pmatrix} \quad 3\text{-}6$$

Here, $1 = xx, 2 = yy, 3 = zz, 4 = yz, 5 = zx, 6 = xy$. Consider the $D_{4h}$ symmetry group of the crystal structure of $FeTe_{1-x}Se_x$ above the structure transition, the elastoresistance matrix can be further simplified by the primary fourfold rotational symmetry, two secondary twofold rotations and two tertiary twofold rotations [36]:

$$m_{ik} = \begin{pmatrix} m_{11} & m_{12} & m_{13} & 0 & 0 & 0 \\ m_{21} & m_{22} & m_{23} & 0 & 0 & 0 \\ m_{31} & m_{32} & m_{33} & 0 & 0 & 0 \\ 0 & 0 & 0 & m_{44} & 0 & 0 \\ 0 & 0 & 0 & 0 & m_{55} & 0 \\ 0 & 0 & 0 & 0 & 0 & m_{66} \end{pmatrix} \quad 3\text{-}7$$

In the following section, we introduce the formalism of the elastoresistivity coefficient $2m_{66}$ as the $B_{2g}$ nematic susceptibility in the $D_{4h}$ symmetry group.

### 3.1.2 *Nematic Order Parameter and Nematic Susceptibility*

We define the nematic order parameter, Φ. Φ is not directly obtained in this experiment but we can assume that it can be expressed as a function of the resistivity anisotropy. The resistivity anisotropy Ψ is defined as:

$$\Psi = \frac{\rho_{xx} - \rho_{yy}}{\rho_{xx} + \rho_{yy}} \quad 3\text{-}8$$

For small value of Ψ, take a Taylor expansion of nematic order parameter Φ. The leading term is linear. Therefore, the small value of resistivity anisotropy in our measurements can be related the nematic order parameter via a proportionality constant c, $\Phi = c\Psi$.

The elastoresistivity coefficient $2m_{66}$ is the derivative of resistivity anisotropy with respect to symmetry breaking strain (the precise definition of elastoresistivity coefficient $2m_{66}$ is described in section 3.1.3):

$$2m_{66} = \frac{d\Psi}{d(\epsilon_{xx} - \epsilon_{yy})} \qquad 3\text{-}9$$

The strain with the same symmetry also couples linearly to Φ, and hence can be considered as a symmetry breaking field conjugate to the electron nematic order parameter. Therefore, we can define the nematic susceptibility $\mathrm{X}_N$ as the quantity that relates the induced order parameter and symmetry breaking strain. For $FeTe_{1-x}Se_x$ sample measured in this project, the sample was oriented with $[110]_T$, therefore, the nematic order parameter and symmetry breaking strain are in $B_{2g}$ symmetry channel. The nematic susceptibility is expressed as[36]:

$$\mathrm{X}_N(B_{2g}) = \left.\frac{d\Phi_{B_{2g}}}{d\epsilon_{xy}}\right|_{\epsilon=0} = cm_{66} \qquad 3\text{-}10$$

Therefore, the elastoresistivity coefficient $2m_{66}$ is related to the nematic susceptibility in $B_{2g}$ symmetry channel via the same proportionality constant c. The constant c depends on the microscopic details of the electronic structure. And the experimental observations of iron pnictides suggest that c is a constant over a wide range of temperature and independent to a certain degree of disorder[38]. Measurement of resistivity cannot distinguish the microscopic degree of freedom, whether it is from the inequivalent occupation in $d_{xz}$ and $d_{yz}$ orbitals suggested by the orbital ordering scenario[39, 40] or from inequivalent antiferromagnetic fluctuations along the $x$ and $y$

direction suggested by the Ising-spin nematic order scenario[41]. Nevertheless, it is a sensitive measure of the electronic nematic order.

### 3.1.3 *Modified Montgomery Method*

We use the modified Montgomery method to measure $\rho_{xx}$, $\rho_{yy}$ of a single crystalline sample. This method first measure the resistances $R_x$, $R_y$ of a square like sample, and then convert $R_x$ and $R_y$ to $\rho_{xx}$, $\rho_{yy}$[42, 43]. As Fig. 3.1 shown, $R_x$, $R_y$ are measured by applying current and measuring voltage via the contacts at the corners of the sample.

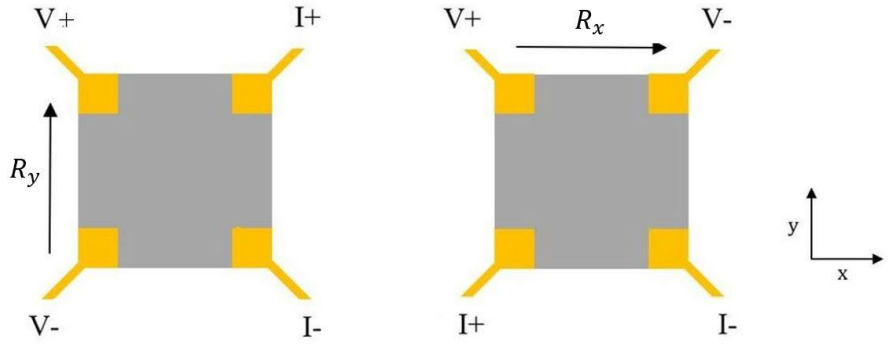


Figure 3.1. The schematic view of samples. The sample was shaped as a square with four contacts at the corners for obtaining the $R_x$ and $R_y$. The position of V- and I+ exchange their positions at one certain temperature by switchbox in order to obtain the values of $R_x$ and $R_y$ in one loop.

The side length $L'_x$ and $L'_y$ of the isotropic equivalent sample are shown as:

$$\frac{L'_x}{L'_y} \approx \frac{1}{2}\left[\frac{1}{\pi} ln \frac{R_y}{R_x} + \sqrt{\left(\frac{1}{\pi} ln \frac{R_x}{R_y}\right)^2 + 4}\right] \qquad 3\text{-}11$$

$R_x$, $R_y$ are the measured resistances along x and y direction respectively at each temperature. The resistivities $\rho_{xx}$ and $\rho_{yy}$ of the sample under strain can be calculated using the equivalent length $L'_x$ and $L'_y$ according to these equations:

$$\rho_{xx} = \frac{\pi}{8}\left(\frac{L_z L_y}{L_z}\right)\left(\frac{L'_x}{L'_y}\right) R_x \sinh\left(\frac{\pi L'_y}{L'_x}\right)$$
$$\rho_{yy} = \frac{\pi}{8}\left(\frac{L_z L_x}{L_y}\right)\left(\frac{L'_y}{L'_x}\right) R_y \sinh\left(\frac{\pi L'_x}{L'_y}\right) \quad 3\text{-}12$$

$L_x$, $L_y$, $L_z$ are the length and thickness of the samples, $R_x$ and $R_y$ are resistance of the sample under strain. Neglecting the small changes in $L_x$ and $L_y$ of the strained sample, the resistivity change of the crystal can be expressed by elastoresistance tensor and strain as:

$$(\Delta\rho/\rho)_{xx} = m_{11}\epsilon_{xx} + m_{12}\epsilon_{yy} + m_{13}\epsilon_{zz} = \epsilon_{xx}(m_{11} - v_p m_{12} - v_s m_{13}) \quad 3\text{-}13$$

$$(\Delta\rho/\rho)_{yy} = \epsilon_{yy}(m_{12} - v_p m_{11} - v_s m_{13}) \quad 3\text{-}14$$

Here, $v_p$ is the Poisson's ratio of the piezoelectric stack, which is a constant defined as $-\epsilon_{yy}/\epsilon_{xx}$. The $v_s = -\epsilon_{zz}/\epsilon_{xx}$ is the effective Poisson's ratio of sample glued on the piezo stack. Because the sample was cut 45 degrees with a, b axes in $[100]_T$ plane, the elastoresistivity tensor $m_{11}$ and $m_{12}$ transform to:

$$m_{1'1'} = m_{11} - 2(m_{11} - m_{12} - 2m_{66})\sin^2\theta\cos^2\theta \quad 3\text{-}15$$

$$m_{1'2'} = m_{12} - 2(m_{11} - m_{12} - 2m_{66})\sin^2\theta\cos^2\theta \quad 3\text{-}16$$

Hence, the normalized resistivity change of sample along x-direction can be given by:

$$(\Delta\rho/\rho)_{xx} = \epsilon_{xx}\left(m_{1'1'} - v_p m_{1'2'} - v_s m_{1'3'}\right) = \epsilon_{xx}\left\{m_{11} - \frac{1}{2}(m_{11} - m_{12} - 2m_{66}) - v_p\left[m_{12} + \frac{1}{2}(m_{11} - m_{12} - 2m_{66})\right] - v_s m_{1'3'}\right\} \quad 3\text{-}17$$

Similarly, the normalized resistivity change along y-direction is:

$$(\Delta\rho/\rho)_{yy} = \epsilon_{yy}\left(m_{1'2'} - v_p m_{1'1'} - v_s m_{1'3'}\right)$$
$$= \epsilon_{yy}\left\{m_{12} + \frac{1}{2}(m_{11} - m_{12} - 2m_{66})\right.$$
$$\left. - v_p\left[m_{11} - \frac{1}{2}(m_{11} - m_{12} - 2m_{66})\right] - v_s m_{1'3'}\right\} \quad 3\text{-}18$$

Combine two equations above:

$$\left(\Delta\rho_{xx} - \Delta\rho_{yy}\right)/\rho = \epsilon_{xx} \cdot 2m_{66}\left(1 + v_p\right) = 2m_{66} \cdot (\epsilon_{xx} - \epsilon_{yy}) \quad 3\text{-}19$$

The normalization factor, $\rho = \sqrt{\rho_{xx}\rho_{yy}}$, is calculated for each sweep using $\rho_{xx}$ and $\rho_{yy}$ values taken at zero anisotropic strain. The dynamic rang of the piezo stack is always not enough to tune through the zero anisotropic strain point, the zero anisotropic strain can be obtained by extrapolating $\rho_{xx}$, $\rho_{yy}$ to the value at which they are equal. We also apply voltage bias during cooling down to tune the zero anisotropic strain approaching to zero strain values, thus compensate some residual isotropic $A_{1g}$ strain.

Then we obtain the elastoresistivity coefficient following:

$$2m_{66} = \left(\left(\Delta\rho_{xx} - \Delta\rho_{yy}\right)/\rho\right)/(\epsilon_{xx} - \epsilon_{yy}) \quad 3\text{-}20$$

### 3.1.4 *Numerical Fits*

The experimental measured elastoresistivity coefficient $2\mathrm{m}_{66}$ as a function of temperature can be fitted to a Curie-Weiss model, which is derived from the phenomenological Ginzburg-Landau theory[36]:

$$2\mathrm{m}_{66} = 2m_{66}^0 + \lambda/[a(T - T^*)] \quad 3\text{-}21$$

Where $T^*$gives the bare mean-field nematic critical temperature at which nematic order would occur if there is no coupling to the crystal lattice[37, 38]. The $\lambda/a$ is the Curie constant[18, 37]. The fitting process was performed by changing the temperature range (lower the high temperature

cutoff and higher the low temperature cutoff between 2K to 300K) until the standard deviation of $2m_{66}^0 + \lambda/[a(T - T^*)]$ is minimized, then $2m_{66}^0$ and $T^*$ be determined.

## 3.2 EXPERIMENTAL TECHNIQUES

### 3.2.1 *Piezoelectric Stack*

We use the piezoelectric stack (P-885.31 Multilayer Piezo Actuator, Piezo Technology Company) to apply strain on samples. As shown in Fig. 3.1, when applying a positive voltage, the piezoelectric stack expands along the polling direction and shrinks in the transverse direction. In our measurement, -20V to 50V voltage bias was applied to the piezo stacks when the temperature is above 150K, -50V to 50V voltage was applied when temperature is below 150K. The amount of strain generated per applied volt changes with temperature, which is an intrinsic property of PZT material. In addition, even at the same temperature, the strain generated per applied voltage depends on whether the piezo stacks are cooled under zero or applied voltage.

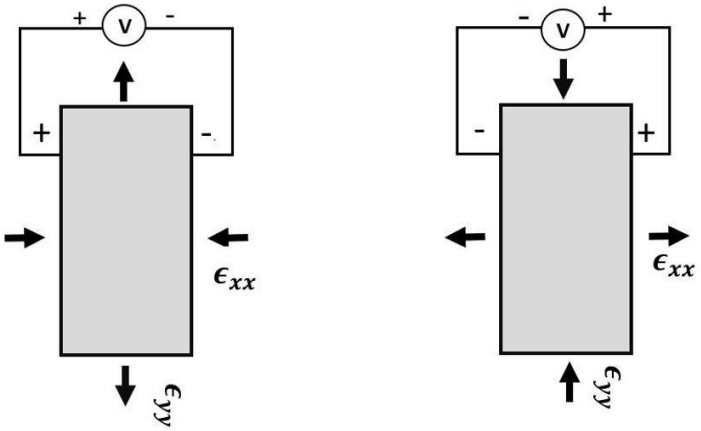


Figure 3.2. The schematic diagram of the piezo stack used in measurement. Under a positive applied voltage, the piezo stacks elongate along the polling direction (y-direction) and shrink along the transverse direction (x-direction).

### 3.2.2 *Strain Gauge*

The strain applied by the piezo stack was measured by a strain gauge attached evenly on the back side of the piezo stack. As Fig. 3.2, it is composed of two sensors vertically stacked that allowed us to obtain the strain along longitudinal (polling) and transverse directions simultaneously. The strain gauge is glued on the back side of the piezo stack because of the limitation from the sample size and the attached electric contacts on the sample. The percent of strain transmitted to the sample was previously assessed by gluing another strain gauge on the top surface of the crystal for $BaFe_2As_2$[44]. For voltage $|V_p| < 50V$, the strain can be fully transmitted in large temperature range.

We obtain the strain from the electronic signals of strain gauge according:

$$\epsilon = \frac{\Delta R/R_0}{Gauge\ Factor} \qquad 3\text{-}22$$

The $R_0 = 350\Omega$ is the origin resistance of strain gauge. $\Delta R$ is the change of resistance at a different temperature obtained by the measured voltage of strain gauge under 1mA constant current. The 1mA constant current through strain gauges is provided by the Stanford Research System Voltage Controlled Current Source. The voltage of strain gauge is measured by an SR830 DSP lock-in amplifier with offset expansion function to increase the sensitivity. The Gauge Factor referred as the resistance change per applied voltage of strain gauge is a constant value (~2.21) pre-characterized by its company. The temperature-dependent change of gauge factor can be ignored in our measurement.

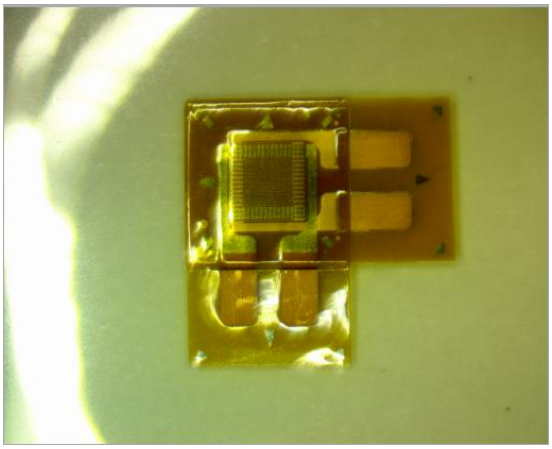

Figure 3.3. The strain gauge attached on the back side of the piezo stack. The vertically stacked two tensors allow us to obtain strain applied by piezo stack along the longitudinal and transverse direction simultaneously. The sensor should be evenly and fully glued with the piezo stack.

### 3.2.3 *Sample Preparation*

The single crystal of the sample is grown by the modified Bridgman method as described in Chapter 2. Crystals were cleaved in thin plates with the shiny surface (in order to maximize the strain transmission). The typical thickness of our samples are between $20\mu m$ to $50\mu m$. In addition, the thickness of the sample has to be homogeneous without isolated holes in order to perform an accurate measurement based on the modified Montgomery method[45]. The cleaved crystal chip was cut 45° along with in-plane a-b axes as a square.

Once the sample was shaped, standard four-point golden contacts were made on the sample by sputtering following the normal procedure. The gold contacts are as small as possible, then connected with the 25μm gold wire using silver epoxy. As Fig. 3.1 show the schematic figure of the sample with four contacts. Through changing the current direction on samples by the switchbox in one temperature loop. The $\rho_{xx}$ and $\rho_{yy}$ can be obtained simultaneously at one temperature setpoint.

### 3.2.4 *Elastoresistance Measurement*

The elastoresistance measurement is performed in Quantum Design Physics Properties Measurement System (PPMS). A Keithley Voltage Supplier was used to apply voltage to the piezoelectric stacks. A Stanford Research System Voltage Controlled Current Source to provide a constant 1mA current to sample measurement. The voltage of the sample and the strain gauge is measured by the SR830 DSP lock-in amplifiers. We increased the measurement sensitivity by using the offset-expand function of the lock-in amplifier, which is especially important when the change of resistance is small. The picture piezoelectric device with a $FeTe_{1-x}Se_x$ crystal mounted for the $B_{2g}$ symmetry channel is shown in Fig. 3. 4.

Normally, we cool down the sample from 300K to 2K at a cooling rate 3K/mins under zero voltage. Starting from 2K, we sweep three voltage loops from -50V to 50V at a rate of 5V/s and switch the current direction by a switchbox at a fixed temperature. As the temperature steps up to 150K, voltage sweep range is changed to -20V to 50V, in order to reduce the risk of piezo stack breaking.

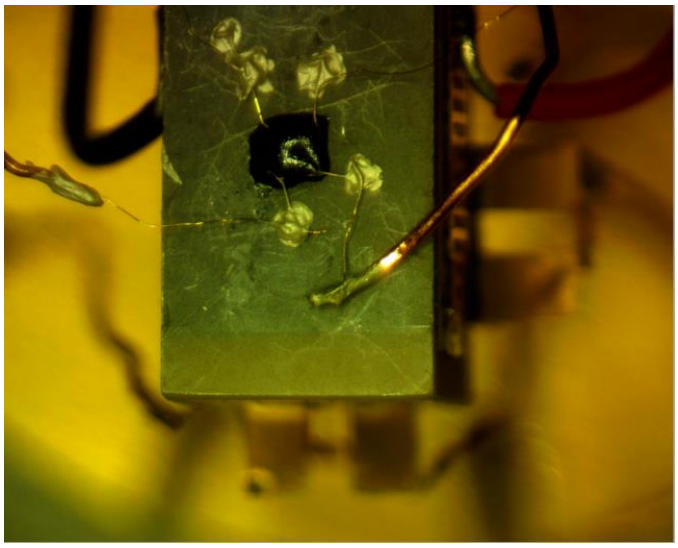

Figure 3.4.The picture of a piezoelectric device for elastoresistance measurement in PPMS. The sample was glued on the front side of the piezo stacks and electrically connected to the voltage leads of the sample puck. The strain gauge was attached on the back side of the piezo stacks to measure the applied strain.

## 3.3 Results and Data Analysis

In this chapter, first, I present the temperature dependent resistivity of all compositions of $FeTe_{1-x}Se_x$ from which we determined the transition temperatures and delineated the phase diagram. I also present the temperature dependent gauge factor, which increases as the temperature decrease. The gauge factor $GF_{xx}$ is larger than $GF_{yy}$ because of the large $A_{1g}$ response. Finally, I present the elastoresistivity coefficient $2m_{66}$ of $FeTe_{1-x}Se_x$ and the Curie-Weiss fitting. Our results show that the nematic fluctuations increase as the Se doping concentration increase for $FeTe_{1-x}Se_x$ (x = 0 - 0.5). The sign of elastoresistivity coefficient $2m_{66}$ flips between the $FeTe_{0.8}Se_{0.2}$ and $FeTe_{0.7}Se_{0.3}$ from negative to positive. The bare nematic critical temperature $T^*$ extracted from the Curie-Weiss fitting is negative for all compositions measured. As the Se doping concentration

increases, the bare nematic critical temperature $T^*$ approaches zero, suggestive of the existence of a nematic quantum critical point at optimal doping.

### 3.3.1 *Freestanding Resistivity*

The freestanding anisotropic resistance $R_{xx}$, $R_{yy}$ measured by the modified Montgomery method was converted to resistivity $\rho_{xx}$, $\rho_{yy}$. Fig. 3.6 shows the temperature dependent resistivity of $FeTe_{0.5}Se_{0.5}$. The anisotropic resistance of the sample is shown as inset. The superconducting transition is sharp, indicating that the excess iron in optimally doped crystal is minimal.

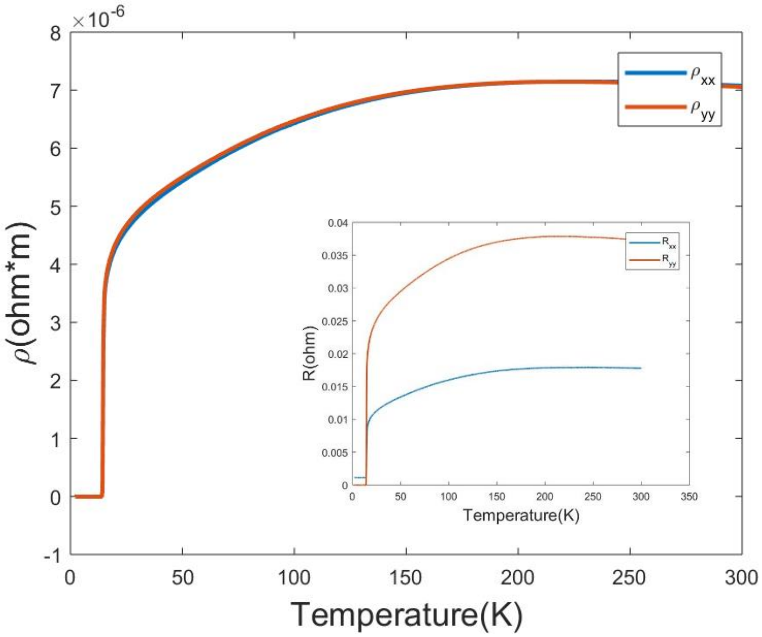


Figure 3.5. The temperature dependent resistivity for freestanding $FeTe_{0.5}Se_{0.5}$ before and after using the Montgomery modified method to covert anisotropic in-plane resistance in equivalent isotropic resistivity.

Fig. 3.6 summarizes the temperature dependence resistivity of $FeTe_{1-x}Se_x$. For FeTe and $FeTe_{0.9}Se_{0.1}$, there is no superconducting transition. The resistivity anomaly associated with paramagnetic-to-antiferromagnetic transition appears at 71K, 36K respectively. For $FeTe_{1-x}Se_x$ (x = 0.2 - 0.5), the excess iron atoms decrease as the Se doping increases, as evidenced by the

vanishing of the resistance upturn. The superconducting $T_c$ is defined as the temperature with the largest slope. The extracted superconducting $T_c$ is listed in the legends of Fig. 3.7.

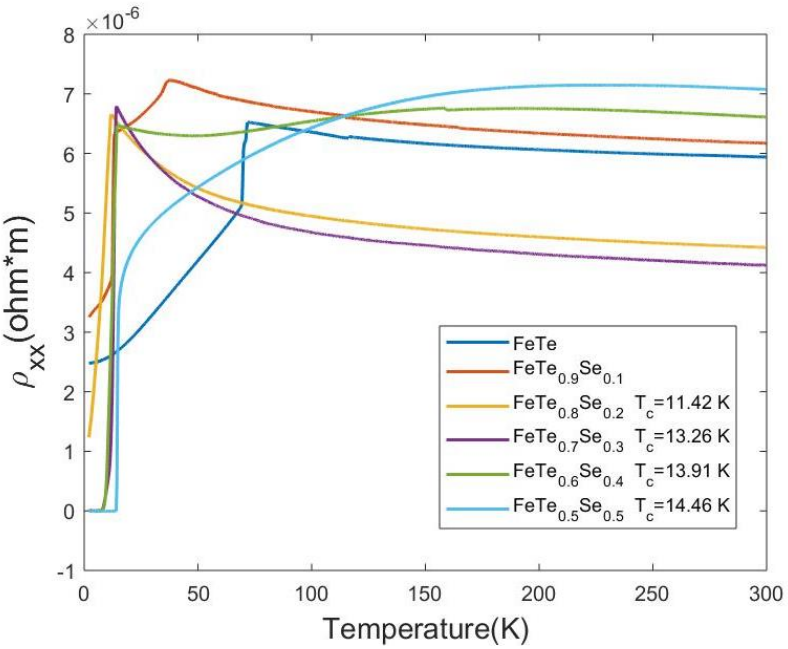


Figure 3.6 The freestanding temperature dependent resistivity $\rho_{xx}$ of $FeTe_{1-x}Se_x$ (x = 0, 0.1, 0.2, 0.3, 0.4, 0.5). The resistivity anomaly associated with the magnetic transition in FeTe and $FeTe_{0.9}Se_{0.1}$ occurs at 71K and 36K respectively. The superconducting $T_c$ is defined as the temperature with the largest slope. The extracted superconducting $T_c$ is listed in the legends.

### 3.3.2 *Gauge Factor of Sample*

In a typical elastoresistance measurement, three voltage loops were swept at one temperature setpoint. Fig. 3.7 shows the resistance of strain gauge subtracted by its offset as a function of applied voltage. The hysteresis is coming from the piezoelectric response of the PZT material, which is not an intrinsic property of the sample.

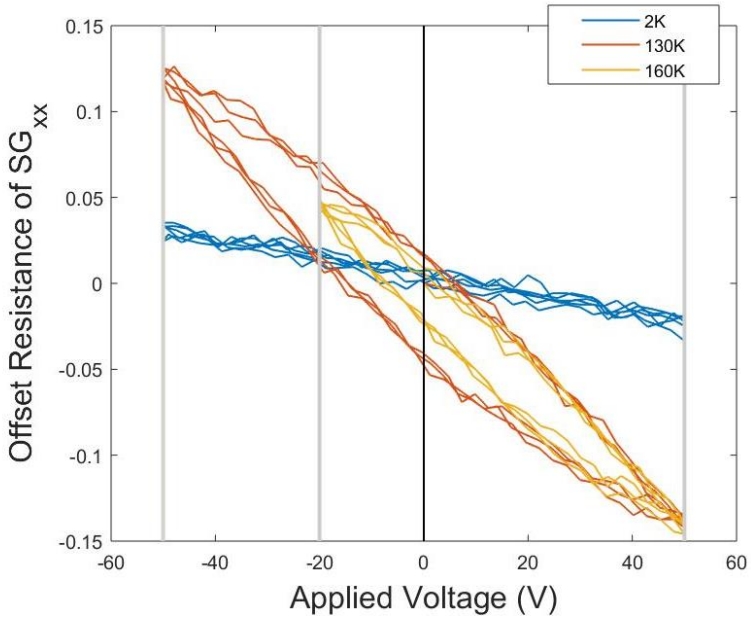


Figure 3.7. The diagram of the resistance subtracted by its offset of a strain gauge along x direction as a function of the applied voltage at 2K, 130K, and 160K.

Fig. 3.8 shows the representative data of the normalized resistivity change of $FeTe_{0.5}Se_{0.5}$ as a function of strain at several temperatures. The solid black lines are their linear fits. The sample has a large resistivity change per applied strain at low temperatures. Since the gauge factor of sample presents the magnitude of the resistivity change per applied strain, it can be directly extracted from the slope of the linear fits:

$$GF_{samplexx} = \frac{\Delta\rho_{xx}/\rho}{\epsilon_{xx}} \qquad 3\text{-}23$$

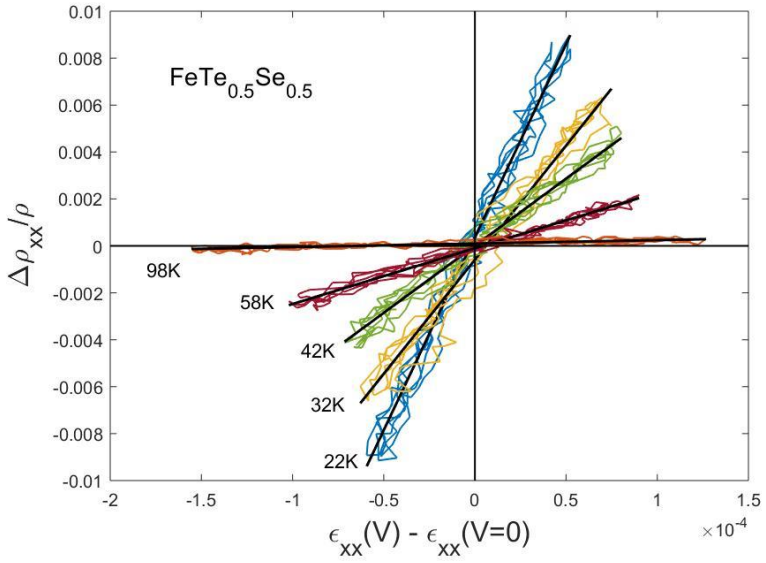


Figure 3.8. The representative data shows the normalized induced resistivity change along x-direction $\Delta\rho_{xx}/\rho$ as a function of strain $\epsilon_{xx}$ at different temperatures for $FeTe_{0.5}Se_{0.5}$. The black lines are their linear fits. The sample has a large resistivity change per applied strain at low temperature.

The $GF_{xx}$ and $GF_{yy}$ of the sample can be obtained simultaneously by the switching the current direction. Fig. 3.9 shows the temperature dependent $GF_{xx}$ and $GF_{yy}$ of $FeTe_{0.5}Se_{0.5}$. The absolute values of both $GF_{xx}$ and $GF_{yy}$ increase as the sample cools down. The much larger absolute value of $GF_{xx}$ comes from the inevitable $A_{1g}$ strain applied to the sample. The negative sign of $GF_{yy}$ means the resistivity along y direction of sample decrease when the $\epsilon_{xx}$ increases.

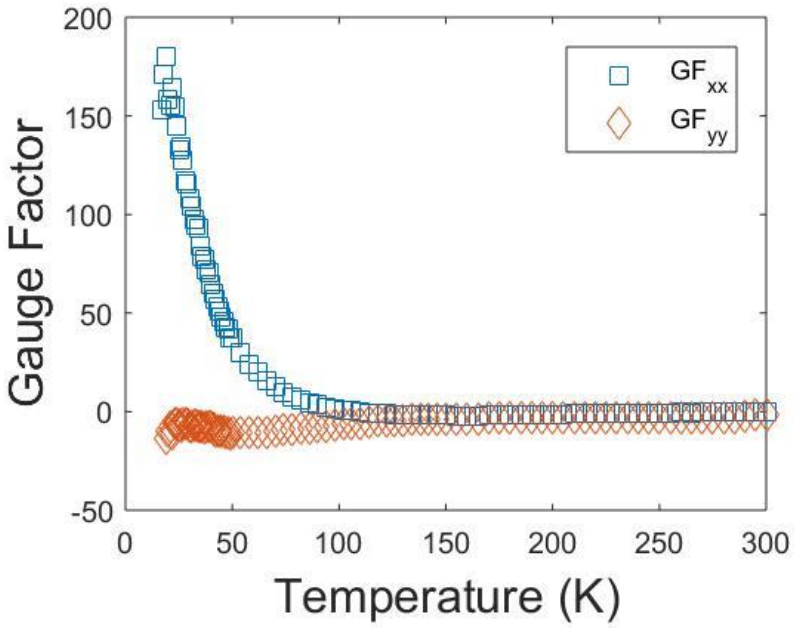


Figure 3.9. The temperature dependent gauge factor $GF_{xx}$ and $GF_{yy}$ of $FeTe_{0.5}Se_{0.5}$. The absolute value of both $GF_{xx}$ and $GF_{yy}$ increases as the sample cools down. The much larger absolute value of $GF_{xx}$ comes from the inevitable $A_{1g}$ strain applied to the sample.

### 3.3.3 *Controlled Cool Down*

As discussed above, the elastoresistivity coefficient $2m_{66}$ is defined as:

$$2m_{66} = \frac{(\Delta\rho_{xx} - \Delta\rho_{yy})}{\rho(\epsilon_{xx} - \epsilon_{yy})} \qquad 3\text{-}24$$

The normalized factor ρ is calculated for each sweep using $\rho_{xx}$ and $\rho_{yy}$ values taken at zero anisotropic strain[18]. However, for measurement of $FeTe_{1-x}Se_x$ in $B_{2g}$ symmetry channel, the dynamic range of the piezo stack is not enough to tune through the zero anisotropic strain point, this is because there is a large built-in strain coming from the mismatch of thermal contraction between $FeTe_{1-x}Se_x$ and the glue and the piezo stacks. In this situation, the zero-strain state can often be obtained by extrapolating $\rho_{xx}, \rho_{yy}$ to the value at which they are equal. However, the

$\rho_{xx}$, $\rho_{yy}$ of $FeTe_{1-x}Se_x$ are far away with each other, extrapolating point may locate in a very large strain range where the resistivity change is not linear with the applied strain.

Here, the controlled cool down method was used to find the zero anisotropic strain. We cool down piezo stacks under the applied voltage to tune the resistivity of glued sample such that its value is close to the resistivity of the freestanding sample. Even we cool down sample under the maximum voltage, the $\rho_{xx}$ and $\rho_{yy}$ are still far to intersect.

### 3.3.4 *Elastoresistivity Coefficient $2m_{66}$*

The elastoresistivity coefficient $2m_{66}$, which measures the nematic susceptibility in $B_{2g}$ symmetry channel, was extracted by the slope of $(\Delta\rho_{xx} - \Delta\rho_{yy})/\rho$ as a function of anisotropic strain $\epsilon_{xx} - \epsilon_{yy}$. Fig. 3.10 shows the representative data of the $(\Delta\rho_{xx} - \Delta\rho_{yy})/\rho$ as a function of anisotropic strain $\epsilon_{xx} - \epsilon_{yy}$ at several temperatures for $FeTe_{0.5}Se_{0.5}$. The black lines are their linear fits. The slope increases as the temperature decreases, which is consistent with the increase of nematic fluctuation of $FeTe_{0.5}Se_{0.5}$ at low temperatures. The red squares in Fig. 3. 11 shows the elastoresistivity coefficient $2m_{66}$ of $FeTe_{0.5}Se_{0.5}$ as a function of temperature from the superconducting critical temperature to 200K. It exhibits a divergent trend at low temperature range.

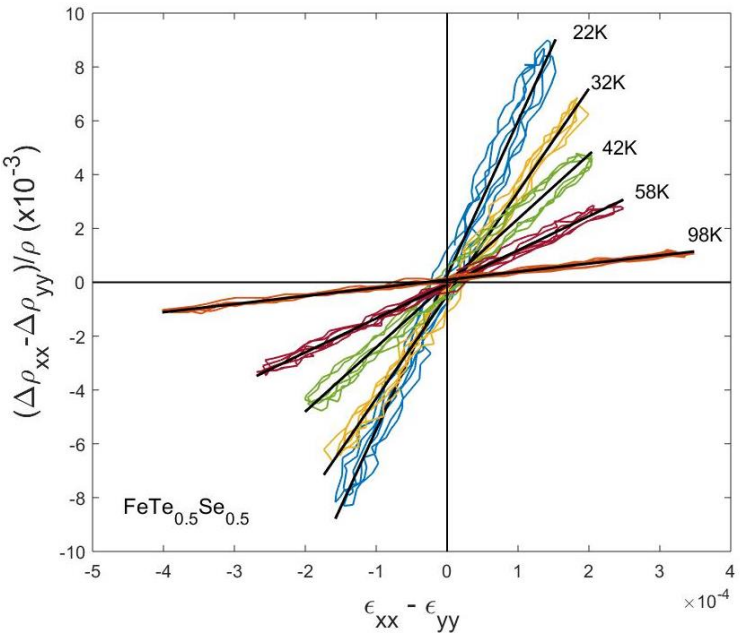


Figure 3.10. The representative $(\Delta\rho_{xx} - \Delta\rho_{yy})/\rho$ as a function of strain anisotropy $\epsilon_{xx} - \epsilon_{yy}$ at several temperatures of $FeTe_{0.5}Se_{0.5}$. The black lines are their linear fits, from which the elastoresistivity coefficient $2m_{66}$ is extracted.

The elastoresistivity coefficient $2m_{66}$ is then fitted to the Curie-Weiss temperature dependence, $2m_{66} = 2m_{66}^0 + \lambda/[a(T - T^*)]$ (Eq. 3-24). The fit range is determined by the method introduced in the last Chapter. The solid black line in Fig. 3.11 is the Curie-Weiss fit of the elastoresistivity coefficient $2m_{66}$. The $2m_{66}$ fit quite well in the temperature range 18-93K with 0.9951 R-square. The bare mean-field nematic critical temperature $T^*$ is -8.37K and the Curie constant $\lambda/a$ is 2395.51. The deviation of $2m_{66}$ from Curie-Weiss behavior at high temperatures may be related to the loss of quasiparticle coherence.

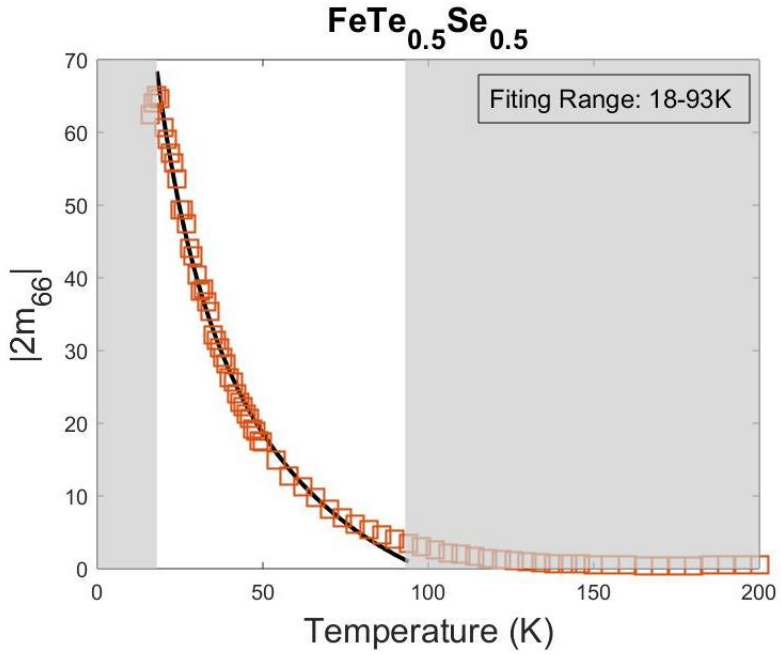


Figure 3.11. Temperature-dependence of elastoresistivity coefficient $2m_{66}$ for $FeTe_{0.5}Se_{0.5}$. The black line is the Curie-Weiss fit. The data fits well in the temperature range 18-93K with a small deviation, characterized by 0.9951 R-square. The bare mean-field nematic critical temperature $T^*$ is -8.37K. The Curie constant $\lambda/a$ is 2395.51.

The elastoresistivity coefficient $2m_{66}$ for all compositions are shown in Fig. 3.12. The data are well fitted by the Curie-Weiss model at a temperature range above $T_c$. Red squares in upper panels shows the experimentally measured value. The $2m_{66}$ is negative for $FeTe_{1-x}Se_x$ (x = 0.2, 0.3) and positive for $FeTe_{1-x}Se_x$ (x = 0.4, 0.5). The absolute value of $2m_{66}$ and hence the strength of nematic fluctuations increases with the Selenium doping. The solid black lines are Curie-Weiss fits. The Curie-Weiss fitting works well in a fitting temperature range. The fit range become narrow as the Se concentration increases. The blue triangles in lower panels show the $|2m_{66} - 2m_{66}^0|^{-1}$, which is proportional to Temperature for a Curie-Weiss law. The black lines are linear fits of $|2m_{66} - 2m_{66}^0|^{-1}$. The yellow circles show $|2m_{66} - 2m_{66}^0|^{-1}(T - T^*)$, which is

expected to be a constant. The horizontal lines are the average of $|2m_{66} - 2m_{66}^0|^{-1}(T - T^*)$ at each temperature.

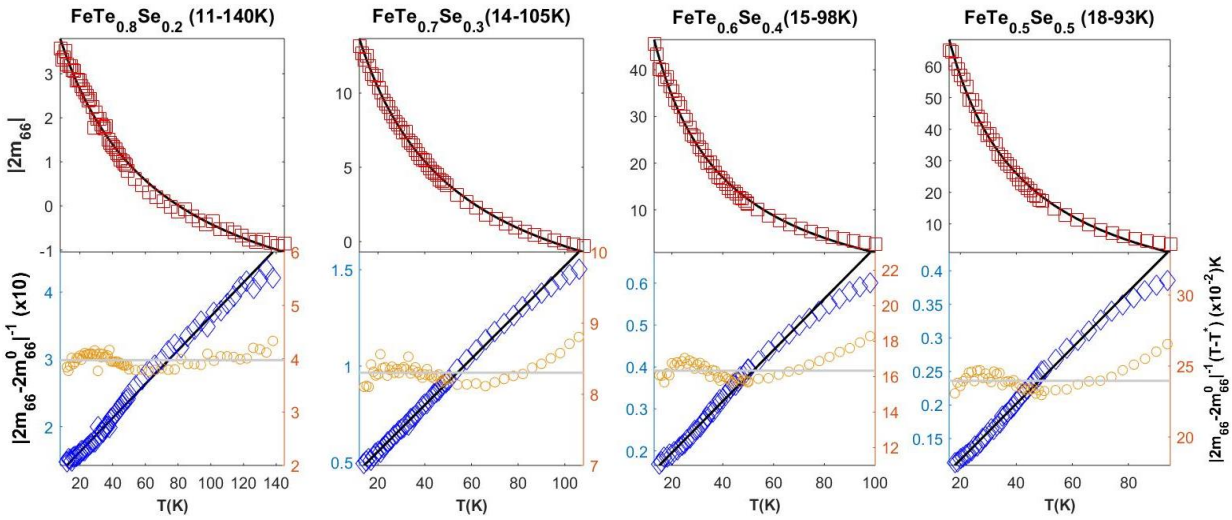


Figure 3.12. Temperature dependent of the $B_{2g}$ symmetry channel elastoresistance $2m_{66}$ of various $FeTe_{1-x}Se_x$ (x = 0.2, 0.3, 0.4, 0.5). (a) $FeTe_{0.2}Se_{0.8}$, (b) $FeTe_{0.3}Se_{0.7}$, (c) $FeTe_{0.4}Se_{0.6}$, (d) $FeTe_{0.5}Se_{0.5}$. The red squares in first-row diagrams stand the experimental measured nematic susceptibility $2m_{66}$ for (a) and (b), $-2m_{66}$ for (c) and (d). The blue diamonds in second-row diagrams stand the $|2m_{66} - 2m_{66}^0|^{-1}$. The black lines are the Curie-Weiss fits of $2m_{66}$ and linear fits of the$|2m_{66} - 2m_{66}^0|^{-1}$respectively. The yellow circles stand the $|2m_{66} - 2m_{66}^0|^{-1}(T - T^*)$ and gray horizontal lines stand the average values of $|2m_{66} - 2m_{66}^0|^{-1}(T - T^*)$ in their fit range.

The divergence of $2m_{66}$ not only reveals the tendency towards the nematic phase transition, but also indicates the increase of nematic fluctuations. Fig. 3.13 shows absolute values of $2m_{66}$ for all $FeTe_{1-x}Se_x$. For clarity, the successive data are offset by 10. For FeTe and $FeTe_{0.9}Se_{0.1}$, $2m_{66}$ increases slightly near the magnetic/structural transition, which may be due to the mixing of $B_{1g}$ symmetry channel. For $FeTe_{1-x}Se_x$ (x = 0.2, 0.3, 0.4, 0.5), the nematic fluctuation increase as the Se doping increase. $2m_{66}$ reaches a maximum for $FeTe_{0.5}Se_{0.5}$, in which there is no sign of structural and magnetic order.

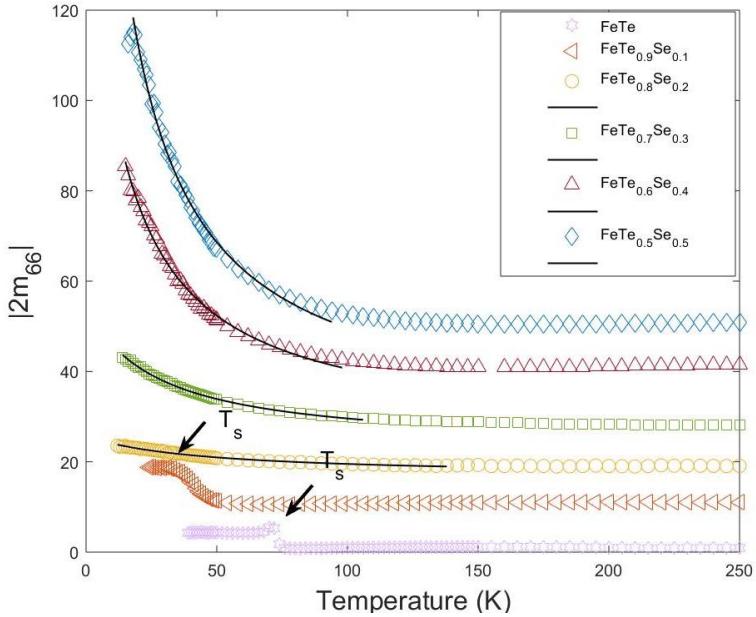


Figure 3.13. Temperature-dependence of elastoresistivity coefficient $|2m_{66}|$ for $FeTe_{1-x}Se_x$. The black solid lines are Curie-Weiss fits. Successive data sets are offset vertically by 10 for clarity.

The Curie-Weiss fitting parameters and the sample dimensions for all compositions are listed in table 3.1. The bare nematic critical temperature $T^*$ is negative for all compositions and increases with the Se concentration. The bare nematic critical temperature of $FeTe_{0.5}Se_{0.5}$ approaches zero. The fit range also becomes narrow as the Se concentration increases. The absolute value of $2m_{66}^0$ increases as the Se content increases.

| Sample | Fit Range(K) | $2m_{66}^{0}$ | $\lambda/a_0\ (K)$ | $T^*(K)$ | Sample Dimension(μm) |
|---|---|---|---|---|---|
| FeTe | / | / | / | / | 59.29×949.75×834.98 |
| $FeTe_{0.9}Se_{0.1}$ | / | / | / | / | 31.75×685.06×681.66 |
| $FeTe_{0.8}Se_{0.2}$ | 11-140 | 3.221 | -397.45 | -44.63 | 22.47×470.25×530.16 |
| $FeTe_{0.7}Se_{0.3}$ | 14-113 | 6.982 | -830.37 | -26.22 | 12.90×1176.25×1176.25 |
| $FeTe_{0.6}Se_{0.4}$ | 15-98 | -14.01 | 1633.83 | -11.98 | 30.54×1058.3×1090.19 |
| $FeTe_{0.5}Se_{0.5}$ | 18-93 | -22.45 | 2395.91 | -8.37 | 59.29×660×570 |

Table 3-1. The Curie-Weiss fitting parameters and sample dimension for all components.

### 3.3.5 *Phase Diagram*

The obtained $T^*$is plotted in the temperature-composition phase diagram of $FeTe_{1-x}Se_x$, as shown in Fig. 3.14. The color map represents the absolute values of elastoresistivity coefficient $2m_{66}$. The strength of nematic fluctuations, measured by $2m_{66}$, is clearly enhanced near the optimal doping. The bare nematic critical temperature $T^*$ is negative for all compositions. Based on the tendency of the $T^*$in our measurements, it can be extrapolated to the finite temperature nematic transition in FeSe at around 80K[46]. The bare nematic critical temperature $T^*$ is approaches to zero for optimally doped $FeTe_{0.5}Se_{0.5}$. Our experimental data and analysis reveal an electronic nematic quantum phase transition occurs at optimally doping compositions. The existence of nematic fluctuations across such a wide temperature and doping range suggests that it is a fundamental ingredient of the normal state of the iron chalcogenide superconductors.

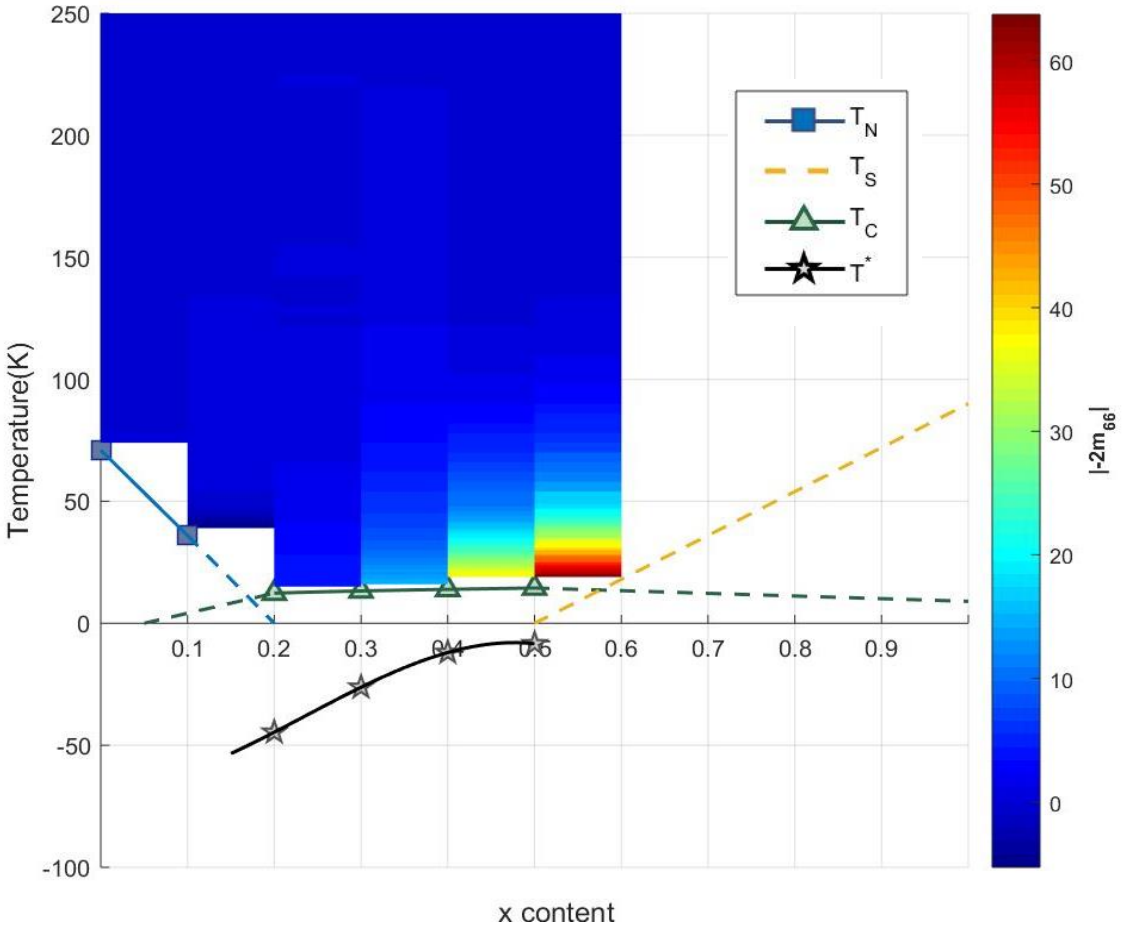


Figure 3.14. The phase diagram of $FeTe_{1-x}Se_x$ (x = 0, 0.1, 0.2, 0.3, 0.4, 0.5). Squares, triangles, and stars indicate the magnetic transition temperature $T_N$, the superconducting transition temperature $T_c$, and the bare nematic critical temperature $T^*$ respectively. The $T^*$ is extracted from the Curie-Weiss fits of $2m_{66}$ in their fitting range. The bare nematic critical temperature $T^*$ is negative for all compositions and approaches zero near optimally doping.

### 3.3.6 *Summary*

The nematic phase plays an important role in the normal state of iron-based superconductors. In this thesis, I have characterized the electronic nematic fluctuations in iron chalcogenide superconductors $FeTe_{1-x}Se_x$ (x = 0, 0.1, 0.2, 0.3, 0.4, 0.5). My primary approach is the elastoresistance technique, which measures the in-plane resistivity anisotropy of a sample under in-situ tunable strain. The elastoresistivity coefficient $2m_{66}$, is proportional to the nematic

susceptibility in $B_{2g}$ symmetry channel of $D_{4h}$ symmetry group. For underdoped $FeTe_{1-x}Se_x$ (x = 0, 0.1), there is a paramagnetic to antiferromagnetic transition accompanied by a tetragonal-to-monoclinic structural transition. We found no evidence for divergent nematic susceptibility in $B_{2g}$ symmetry channel in these underdoped samples. For $FeTe_{1-x}Se_x$ (x = 0.2, 0.3, 0.4, 0.5), the nematic susceptibility diverges at low temperatures. The temperature dependence of $2m_{66}$ is well fitted to a Curie-Weiss model. The Curie-Weiss constant increases as the Se doping concentration increases and reaches a maximum at the optimal doping x = 0.5. The bare nematic critical temperature $T^*$ is negative for all compositions and also approaches zero at the optimal doping x = 0.5. All the data is consistent with the existence a nematic quantum critical point and enhanced nematic fluctuations near optimal doping, which could be extrapolated from the finite-temperature nematic transition in FeSe.

The origin of the sign flipping of $2m_{66}$ (the nematic coefficient $2m_{66}$ are negative for x = 0.2, 0.3, positive for x = 0.4, 0.5) is unknown. It may be related to the change of electronic structure as a function of doping, which requires further investigation. In principle, the elastoresistivity measurement is capable of measuring other symmetry channel, such as $A_{1g}$ and $B_{1g}$. These measurements probe fluctuations associated with other degrees of freedom or other symmetry breaking phases. Future experiments of this kind will help establish a comprehensive understanding of the nematic phase and the superconductivity of iron chalcogenide superconductors.

# BIBLIOGRAPHY


1. Kamihara, Y., et al., *Iron-based layered superconductor La[O(1-x)F(x)]FeAs (x = 0.05-0.12) with T(c) = 26 K.* J Am Chem Soc, 2008. **130**(11): p. 3296-7.
2. Ando, Y. and K. Segawa, *Magnetoresistance of untwinned YBa(2)Cu(3)O(y) single crystals in a wide range of doping: anomalous hole-doping dependence of the coherence length.* Phys Rev Lett, 2002. **88**(16): p. 167005.
3. Chen, G.F., et al., *Superconductivity at 41 K and its competition with spin-density-wave instability in layered CeO1-xFxFeAs.* Phys Rev Lett, 2008. **100**(24): p. 247002.
4. Chen, X.H., et al., *Superconductivity at 43 K in SmFeAsO1-xFx.* Nature, 2008. **453**(7196): p. 761-2.
5. Ren, Z.A., et al., *Superconductivity at 55K in iron-based F-doped layered quaternary compound Sm[O(1-x)F(x)]FeAs.* Chinese Physics Letters, 2008. **25**(6): p. 2215-2216.
6. Ren, Z.A., et al., *Superconductivity in the iron-based F-doped layered quaternary compound Nd[O(1-x)F(x)]FeAs.* Epl, 2008. **82**(5).
7. Liu, K., Z.-Y. Lu, and T. Xiang, *Atomic and electronic structures of FeSe monolayer and bilayer thin films on SrTiO3(001): First-principles study.* Physical Review B, 2012. **85**(23).
8. Shi, H., et al., *Magnetic behavior of Fe(Se,Te) systems: First-principles calculations.* Journal of Applied Physics, 2011. **110**(4).
9. Singh, D.J. and M.H. Du, *Density functional study of LaFeAsO(1-x)F(x): a low carrier density superconductor near itinerant magnetism.* Phys Rev Lett, 2008. **100**(23): p. 237003.
10. Qian, T., et al., *Absence of a holelike fermi surface for the iron-based K0.8F1.7Se2 superconductor revealed by angle-resolved photoemission spectroscopy.* Phys Rev Lett, 2011. **106**(18): p. 187001.
11. Zhang, Y., et al., *Nodeless superconducting gap in A(x)Fe2Se2 (A=K,Cs) revealed by angle-resolved photoemission spectroscopy.* Nat Mater, 2011. **10**(4): p. 273-7.
12. Chen, X.H., et al., *Iron-based high transition temperature superconductors.* National Science Review, 2014. **1**(3): p. 371-395.
13. Alireza, P.L., et al., *Superconductivity up to 29 K in SrFe(2)As(2) and BaFe(2)As(2) at high pressures.* J Phys Condens Matter, 2009. **21**(1): p. 012208.
14. Rotter, M., et al., *Spin-density-wave anomaly at 140 K in the ternary iron arsenideBaFe2As2.* Physical Review B, 2008. **78**(2).
15. Sefat, A.S., et al., *Superconductivity at 22 K in Co-doped BaFe2As2 crystals.* Phys Rev Lett, 2008. **101**(11): p. 117004.
16. Subedi, A., et al., *Density functional study of FeS, FeSe, and FeTe: Electronic structure, magnetism, phonons, and superconductivity.* Physical Review B, 2008. **78**(13).
17. Fradkin, E., et al., *Nematic Fermi Fluids in Condensed Matter Physics.* Annual Review of Condensed Matter Physics, 2010. **1**(1): p. 153-178.
18. Chu, J.H., et al., *In-plane resistivity anisotropy in an underdoped iron arsenide superconductor.* Science, 2010. **329**(5993): p. 824-6.
19. Tanatar, M.A., et al., *Uniaxial-strain mechanical detwinning of CaFe2As2 and BaFe2As2 crystals: Optical and transport study.* Physical Review B, 2010. **81**(18).
20. Fernandes, R.M., A.V. Chubukov, and J. Schmalian, *What drives nematic order in iron-based superconductors?* Nature Physics, 2014. **10**(2): p. 97-104.

21. Fang, C., et al., *Theory of electron nematic order in LaFeAsO.* Physical Review B, 2008. **77**(22).
22. Xu, C., M. Müller, and S. Sachdev, *Ising and spin orders in the iron-based superconductors.* Physical Review B, 2008. **78**(2).
23. Chen, C.C., et al., *Finite-temperature spin dynamics and phase transitions in spin-orbital models.* Physical Review B, 2009. **80**(18).
24. Lv, W., J. Wu, and P. Phillips, *Orbital ordering induces structural phase transition and the resistivity anomaly in iron pnictides.* Physical Review B, 2009. **80**(22).
25. Yildirim, T., *Strong coupling of the Fe-spin state and the As-As hybridization in iron-pnictide superconductors from first-principle calculations.* Phys Rev Lett, 2009. **102**(3): p. 037003.
26. Christianson, A.D., et al., *Unconventional superconductivity in Ba(0.6)K(0.4)Fe2As2 from inelastic neutron scattering.* Nature, 2008. **456**(7224): p. 930-2.
27. Inosov, D.S., et al., *Normal-state spin dynamics and temperature-dependent spin-resonance energy in optimally doped BaFe1.85Co0.15As2.* Nature Physics, 2009. **6**(3): p. 178-181.
28. Li, S., et al., *First-order magnetic and structural phase transitions inFe1+ySexTe1−x.* Physical Review B, 2009. **79**(5).
29. Chiheng Dong, H.W., Zujuan Li, Jian Chen, H. Q. Yuan, and Minghu Fang, *Revised phase diagram for the FeTe1-xSex system with fewer excess Fe atoms.* Physical Review B, 2011. **84**: p. 224506.
30. Liu, X., et al., *Electronic structure and superconductivity of FeSe-related superconductors.* J Phys Condens Matter, 2015. **27**(18): p. 183201.
31. Sales, B.C., et al., *Bulk superconductivity at 14 K in single crystals ofFe1+yTexSe1−x.* Physical Review B, 2009. **79**(9).
32. Kawasaki, Y., et al., *Phase diagram and oxygen annealing effect of FeTe1−xSex iron-based superconductor.* Solid State Communications, 2012. **152**(13): p. 1135-1138.
33. Singh, D.J., *Superconductivity and magnetism in 11-structure iron chalcogenides in relation to the iron pnictides.* Sci Technol Adv Mater, 2012. **13**(5): p. 054304.
34. Fang, M.H., et al., *Superconductivity close to magnetic instability inFe(Se1−xTex)0.82.* Physical Review B, 2008. **78**(22).
35. Ding, M.C., H.Q. Lin, and Y.Z. Zhang, *Hidden (pi,0) instability as an itinerant origin of bicollinear antiferromagnetism in Fe1+x Te.* Physical Review B, 2013. **87**(12).
36. Hsueh-Hui Kuo, J.-H.C., Johnana C. Palmstrom, Steven A. Kivelson, Ian R. Fisher, *Ubiquitous signatures of nematic quantum criticality in optimally doped Fe-based superconductors.* Science, 2016. **352**(6288): p. 958-962.
37. Kuo, H.-H., et al., *Measurement of the elastoresistivity coefficients of the underdoped iron arsenide Ba(Fe0.975Co0.025)2As2.* Physical Review B, 2013. **88**(8).
38. Kuo, H.H. and I.R. Fisher, *Effect of disorder on the resistivity anisotropy near the electronic nematic phase transition in pure and electron-doped BaFe(2)As(2).* Phys Rev Lett, 2014. **112**(22): p. 227001.
39. Chen, C.C., et al., *Orbital order and spontaneous orthorhombicity in iron pnictides.* Physical Review B, 2010. **82**(10).
40. Lv, W.C. and P. Phillips, *Orbitally and magnetically induced anisotropy in iron-based superconductors.* Physical Review B, 2011. **84**(17).

41. Fernandes, R.M., E. Abrahams, and J. Schmalian, *Anisotropic In-Plane Resistivity in the Nematic Phase of the Iron Pnictides.* Physical Review Letters, 2011. **107**(21).
42. dos Santos, C.A.M., et al., *Procedure for measuring electrical resistivity of anisotropic materials: A revision of the Montgomery method.* Journal of Applied Physics, 2011. **110**(8).
43. Montgomery, H.C., *Method for Measuring Electrical Resistivity of Anisotropic Materials.* Journal of Applied Physics, 1971. **42**(7): p. 2971-2975.
44. Jiun-Haw Chu, H.-H.K., James G. Analytis, Ian R. Fisher, *Divergent nematic susceptibility in an iron arsenide superconductors.* Science, 2012. **337**.
45. Pauw, L.J.v.d., *A method of measuring specific resistivity and hall effect of discs of abritrary shape.* Philips Res. Repts, 1958. **13**: p. 1-9.
46. M. D. Watson, T.K.K., A. A. Haghighirad. N. R. Davies, A. McCollam, A. Narayanan, S. F. Blake, Y. L. Chen at el., *Emergence of the nematic electronic state in FeSe.* PhysRevB, 2015. **91**.